

Supplementary Material

1 SUPPLEMENTARY FIGURES

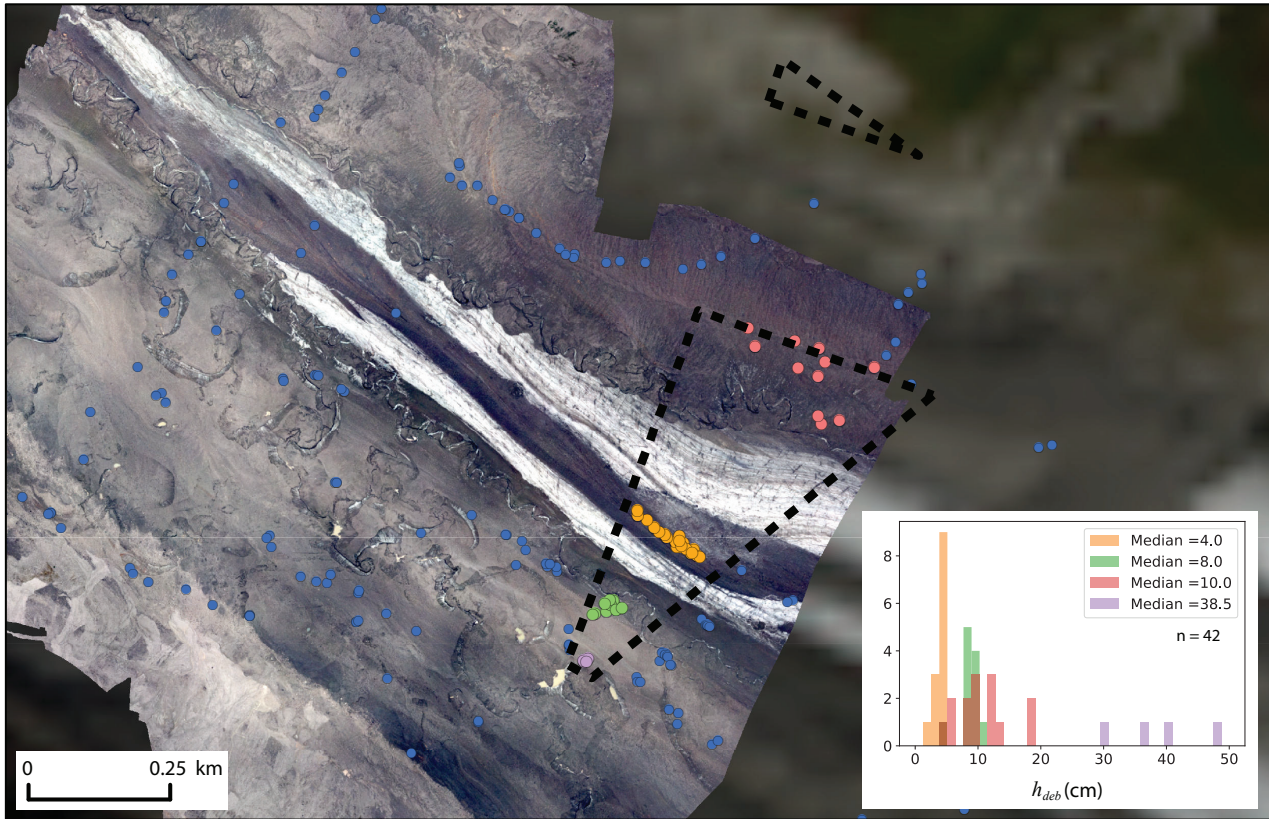


Figure S1: Debris thickness measurement locations within the study domain (black dashed line), color coordinated by image segment (Fig. 1, main text) with debris thickness measurements shown in the inset histogram. For each measurement, between 1 and 5 point debris thickness measurements were made in a few meter radius and averaged. Blue points show the debris thickness measurements made in the years leading up to this study in an effort to find an ideal setting for this experiment. The median 10 cm debris thickness segment contained the side of a medial moraine at/near the angle of repose with a thinly debris covered/newly forming ice cliff. Because of this variability, this segment was not used beyond its inclusion in Fig. 4. The fewest debris thickness measurements were made at the median 38.5 cm site (rounded down for analysis). There was the largest variability here because of larger clasts at the surface. I made fewer measurements at this segment because it was small in the foreground of the thermal image and I did not want to disturb the debris more than I needed to within the thermal image since replacing a 38 cm excavation is still thermally disruptive. From the excavations made however, it was apparent that the area in frame had a stable debris thickness with variable larger clasts on top (visible in Supplemental Video 1).

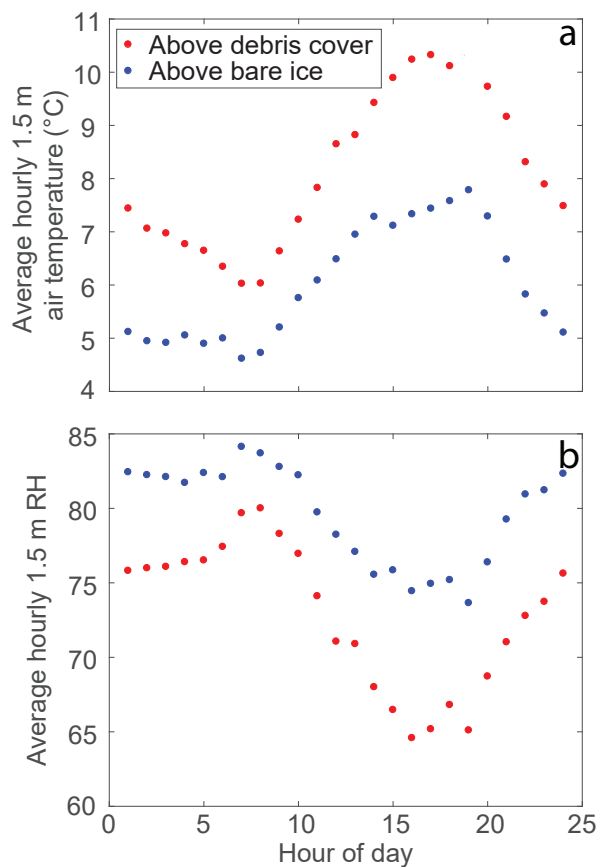


Figure S2: 1.5 m air temperature (a) and *RH* (b) collected above both a debris-covered and bare glacier ice surface between July 31, 2012 23:42 to August 30, 2012 20:14 AKDT at the approximate locations (1) and (5) in Fig. 1 (main article), respectively. Shown here as hourly averages for the full duration of the interval. These data were used to compute a set of correction factors to adjust 2016 measurements of 1.5 m air temperature above a debris-covered surface to approximate the air temperature above bare-ice.

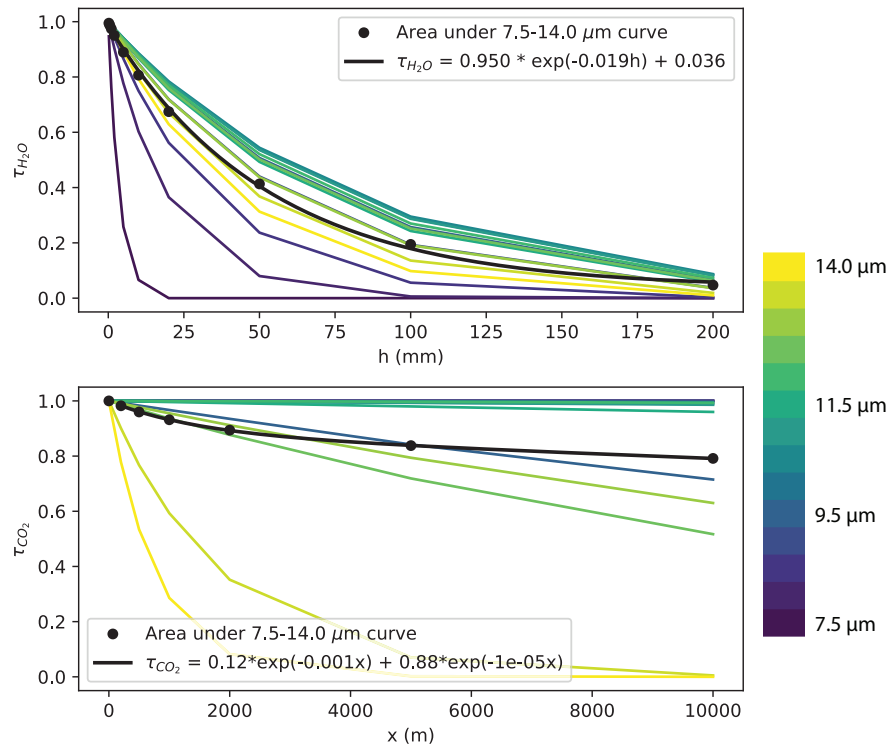


Figure S3: Summary of the Passman-Larmore tables that prescribe values of τ_{H_2O} and τ_{CO_2} given h and x , respectively, and λ for both. For each h and x where data are present, numerical integration was used to find a total value of attenuation over a range of λ specific to the thermal camera used in this study (7.5-14.0 μm). Nonlinear ordinary least squares regression was used to find a function form of signal attenuation for both τ_{H_2O} and τ_{CO_2} .

2 SUPPLEMENTARY TABLE

Table S1. Model parameter values calibrated at Canwell Glacier, Alaska, USA between August 1st and August 17th, 2016 within the observation windows described in Sect. 3.1 and shown in Fig. 5. The units for glacier melt rate that these coefficients correspond to are cm per hour.

	This study			Following Rowan et al. (2021)			Following Rounce et al. (2021)		
Debris thickness									
Model parameter	a_9	-	-	a_{10}	b_{10}	-	a_{11}	b_{11}	c_{11}
10th percentile	7.2			9.0×10^{-8}	-7.8		9.7	2.1	0.5
Median	8.0			5.1×10^{-4}	-5.0		15.1	7.9	0.5
90th percentile	9.0			0.1	-3.0		24.3	20.0	0.5
Sub-debris melt									
Model parameter	a_{12}	a_{13}	b_{13}				a_{14}	-	-
10th percentile	0.7×10^{-1}	1.5×10^{-2}	0.1				0.2		
Median	1.3×10^{-1}	2.5×10^{-2}	0.2				0.4		
90th percentile	1.7×10^{-1}	3.9×10^{-2}	0.4				0.8		

3 SUPPLEMENTARY DATA

3.1 Supplemental Video 1

Glacier selfie stick time-lapse camera footage of locations where sub-daily melt rates were measured: bare glacier ice, location (5) in Fig. 1; 4 cm debris thickness (4); 8 cm debris thickness (2); and 38 cm debris thickness (1). Where the camera position was significantly altered, a correction in the melt rate and cumulative melt signal was made. When the length of ablation stake exposed above the surface exceeded the graduation tape, small abrasions and stable specs of silt/dirt were used to make distance measurements where possible. The bare ice ablation stake was re-drilled twice due to melt rates exceeding the length of the stake.

3.2 Supplemental Video 2

The thermal images where segment surface temperature medians and percentile statistics were extracted (top left). A histogram of all temperature values in frame is shown on the left side of the thermal image (both the thermal image and histogram are displayed on the same temperature scale. Segments are color coded to agree with the Figures in the main article and all aspects of the video: blue, bare glacier ice at Fig. 1 location (5); orange, 4 cm debris thickness (4); green, 8 cm debris thickness (2); purple, 38 cm debris thickness (1); and red, off-glacier valley wall (7). The panel on the top right shows the median temperature values extracted from the thermal image for each image segment (Fig. 1) plotted against segment debris thickness and melt rate measurements coincident in time also plotted against the corresponding image segment debris thickness. The red dot is the temperature of the off-glacier, southwest facing valley wall. Of the four time-series panels, the top three show the thermal image derived surface temperature (dots color corresponds to segment) as well as sub-debris temperature profiles measured with contact thermistors in 4 cm increments from the debris-ice interface to the surface. The bottom time-series shows precipitation for context, measured next to the thermal camera. The current frame is identified by a vertical red line.

3.3 Supplemental Video 3

Model results comparing methods. This study (turquoise), debris thickness (Eq. 9), sub-debris melt (Eq. 13); Rounce et al. (2021) (yellow-green), debris thickness (Eq. 11), sub-debris melt (Eq. 14); and Rowan et al. (2021) (grey), debris thickness (Eq. 10). Measurements are plotted as black dots. The time interval is the same as Fig. 5.

3.4 Supplemental Video 4

Same as Supplemental Video 2, except the panel on the top right shows: measured melt (colored dots, black line); valley wall surface temperature extracted from the thermal image (red cross) and thermistor surface temperature measured in frame of the thermal image at 38 cm debris thickness (purple cross), both possible input for T_s^* (here, the thick debris, thermistor data is used); modeled surface temperature (this study, Eq. 12, dashed light blue line); modeled melt (this study, Eq. 13, solid light blue line); and modeled melt (Rounce et al. (2021), Eq. 14, solid yellow line). The four time-series panels show the respective cumulative glacier melt for each debris thickness corresponding to the color coded thermal image segments. Black dots and triangles are melt measurements from the selfie stick method and manual field measurements, respectively. The light blue line is modeled melt from this study and the dashed yellow line is modeled following Rounce et al. (2021).

4 APPENDIX: ATMOSPHERIC TRANSMITTANCE

Atmospheric transmittance, τ_{atm} , can be estimated by solving for molecular absorption of water vapor, τ_{H_2O} , molecular absorption of carbon dioxide, τ_{CO_2} and signal attenuation from scattering by particles in the atmosphere, τ_s (Gaussorgues, 1994). In the following equations, near-surface atmospheric temperature, T_{atm} , and relative humidity, RH , over debris cover and bare ice (differences shown in Fig. S2) were used to derive specific humidity, q_v , and moist air density, ρ , specific to two settings: over bare ice (q_{vice} and ρ_{ice}) and over debris (q_{vdeb} and ρ_{deb}). Building from the August-Roche-Magnus approximation of the Clausius-Clapeyron relation to derive saturation vapor pressure $e_s(T_{atm})$ (Pa),

$$e_s(T_{atm}) = 6.11 \exp\left(\frac{17.625T_{atm}}{T_{atm} + 243.04}\right), \quad (S1)$$

q_v is approximated from the following standard equations:

$$e = RH * e_s(T_{atm}) \quad (S2)$$

$$w = \frac{eR_d}{R_v(p - e)} \quad (S3)$$

$$q_v = \frac{w}{w + 1} \quad (S4)$$

where e is partial pressure of water vapor (Pa), w is the mass mixing ratio of water vapor to dry air (dimensionless), R_d is the specific gas constant for dry air ($287.058 \text{ J kg}^{-1} \text{ K}^{-1}$), R_v is the specific gas constant for water vapor ($461.5 \text{ J kg}^{-1} \text{ K}^{-1}$) and p is atmospheric pressure (Pa). Static measurements of p were made in the field ($p = \sim 87000 \text{ Pa}$) with a Kestrel 4000 Weather Meter.

Finally, ρ is defined as,

$$\rho = \frac{p}{R_d T_{atm}} \left(1 - 0.378 \frac{e}{p}\right). \quad (S5)$$

This set of equations allowed the computation of h from Eq. 5, accounting for unique atmospheres for every thermal image segment over debris cover and bare ice proportional to the distance these two conditions were present along x (Fig. 1c). Spectral transmittance through the atmosphere considering molecular absorption of water vapor, τ_{H_2O} , can now be extracted from experimentally derived Passman-Larmore tables (Passman and Larmore, 1956; Gaussorgues, 1994). Passman-Larmore tables derive τ_{H_2O} as a function of h for single wavelengths (λ). Because the thermal camera used in this study acquired data over a spectral range, a single value of τ_{H_2O} was computed using Simpson's rule to numerically integrate over a spectral range from λ_1 to λ_2 (μm) for each h

$$\tau_{H_2O}(h) = \int_{\lambda_1}^{\lambda_2} \tau_{H_2O}(\lambda) d\lambda. \quad (S6)$$

A nonlinear ordinary least squares regression of $\tau_{H_2O}(h)$ for each h in in the Passman-Larmore table provided a functional form of τ_{H_2O} over the camera specific spectral range $\lambda_1 = 7.5$ to $\lambda_2 = 14.0\mu m$,

$$\tau_{H_2O}(7.5 - 14\mu m) = 0.930 \exp(-0.021h) + 0.046. \quad (S7)$$

Passman-Larmore tables also provide experimental values of spectral transmittance through the atmosphere considering molecular absorption of gaseous carbon dioxide, τ_{CO_2} , as a function of λ and a horizontal distance, in the case of this study, x (m). Following a similar formulation to Eq. S6, and identical numerical methods, a single value of τ_{CO_2} was computed over the spectral range λ_1 to λ_2 ,

$$\tau_{CO_2}(x) = \int_{\lambda_1}^{\lambda_2} \tau_{CO_2}(\lambda) d\lambda. \quad (S8)$$

Figure S3 shows a summary of the Passman-Larmore table data, the derived integrated values at each h or x for τ_{H_2O} and τ_{CO_2} , respectively, and the derived functional forms of these data used to extract attenuation values for any h or x value below 200 mm and 10 km, respectively (the complete table is included, yet this study did not consider a distance beyond 1 km).

A nonlinear ordinary least squares regression of $\tau_{CO_2}(x)$ for each x provided in the Passman-Larmore table produced the following two term exponential functional form of τ_{CO_2} specific to $\lambda_1 = 7.5$ to $\lambda_2 = 14.0\mu m$,

$$\tau_{CO_2}(7.5 - 14\mu m) = 0.12 \exp(-0.001x) + 0.88 \exp(-0.00001x) \quad (S9)$$

Signal attenuation from scattering by particles in the atmosphere, τ_s , along x was found by numerical integration over $\lambda_1 = 7.5$ to $\lambda_2 = 14.0\mu m$, of a relation given in Gaussorgues (1994),

$$\tau_s = \int_{\lambda_1}^{\lambda_2} \exp(-\gamma_\lambda x) d\lambda, \quad (S10)$$

where γ_λ , the scattering coefficient, is defined as

$$\gamma_\lambda = 0.0002 \left(\frac{0.6}{\lambda} \right)^{1.3}. \quad (S11)$$

The exponent 1.3 is an experimental parameterization of Rayleigh scattering from mists or suspended condensed water droplets in the near surface atmosphere during clear visibility (20 km) conditions (Gaussorgues, 1994).

REFERENCES

- Gaussorgues, G. (1994). *Infrared thermography* (Springer: Berlin/Heidelberg, Germany)
- Passman, S. and Larmore, L. (1956). *Atmospheric transmission*. Tech. rep., Rand Corp Santa Monica CA
- Rounce, D. R., Hock, R., McNabb, R., Millan, R., Sommer, C., Braun, M., et al. (2021). Distributed global debris thickness estimates reveal debris significantly impacts glacier mass balance. *Geophysical Research Letters* 48, e2020GL091311

Rowan, A. V., Nicholson, L. I., Quincey, D. J., Gibson, M. J., Irvine-Fynn, T. D., Watson, C. S., et al. (2021). Seasonally stable temperature gradients through supraglacial debris in the everest region of nepal, central himalaya. *Journal of Glaciology* 67, 170–181